



UNIVERSITY OF LEEDS

This is a repository copy of *Large Eddy Simulation of Deposition of Anisotropic Particles in a Turbulent Channel Flow*.

White Rose Research Online URL for this paper:
<http://eprints.whiterose.ac.uk/111273/>

Version: Accepted Version

Proceedings Paper:

Njobuenwu, DO orcid.org/0000-0001-6606-1912 and Fairweather, M (2014) Large Eddy Simulation of Deposition of Anisotropic Particles in a Turbulent Channel Flow. In: Proceedings of the 10th International ERCOFTAC Symposium on Engineering Turbulence Modelling and Measurements – ETMM10. 10th International ERCOFTAC Symposium on Engineering Turbulence Modelling and Measurements – ETMM10, 17-19 Sep 2014, Don Carlos Resort, Marbella, Spain. .

Reuse

Unless indicated otherwise, fulltext items are protected by copyright with all rights reserved. The copyright exception in section 29 of the Copyright, Designs and Patents Act 1988 allows the making of a single copy solely for the purpose of non-commercial research or private study within the limits of fair dealing. The publisher or other rights-holder may allow further reproduction and re-use of this version - refer to the White Rose Research Online record for this item. Where records identify the publisher as the copyright holder, users can verify any specific terms of use on the publisher's website.

Takedown

If you consider content in White Rose Research Online to be in breach of UK law, please notify us by emailing eprints@whiterose.ac.uk including the URL of the record and the reason for the withdrawal request.



eprints@whiterose.ac.uk
<https://eprints.whiterose.ac.uk/>

Large Eddy Simulation of Deposition of Anisotropic Particles in a Turbulent Channel Flow

D.O. Njobuenwu and M. Fairweather

Institute of Particle Science and Engineering, School of Process, Environmental and Materials Engineering, University of Leeds, Leeds LS2 9JT, UK

d.o.njobuenwu@leeds.ac.uk

1 Introduction

The deposition of solid suspensions on the surface of a wall is of great importance in many applications such as the deposition of corrosion oxides in the form of CRUD (corrosion residual unidentified deposit) in nuclear reactors, and the fouling of heat exchangers and turbine blades (Njobuenwu and Fairweather, 2012), to mention a few. In nuclear reactor applications, for example, in-circuit dusts from metal surfaces exposed to gaseous coolant are small in size, but these corrosion products agglomerate into larger particles giving rise to a wide range of sizes and shapes which can eventually deposit on the boiler tubes or fuel cladding, creating concerns that impact on safety, thermal efficiency and fuel performance (Hazelton, 1987).

Particle deposition for the non-interacting regime is defined here as the process of attaching suspended particles from a fluid in motion to the surface of a wall, with no detachment of the deposit occurring. Liu and Agarwal (1974) studied particle deposition by measuring the dependence of the rate of particle transport, in velocity units, to the surface on the particle response time. The particle response time is the time required for the particle to respond to the changes in the carrier fluid velocity and it depends on the particle size, shape, density and the carrier fluid viscosity.

Liu and Agarwal (1974) measured the transport of olive oil droplets of 1.4 to 21 μm diameter and a density ratio of 770 from a turbulent air flow to the internal wall of a smooth glass pipe for bulk flow Reynolds numbers of 10,000 and 50,000. The measured particle deposition velocity rate u_d^+ and the particle relaxation time τ_p^+ , both in wall units, was reported as a universal curve in which three distinct deposition regimes were noted. Sub-micron particle ($\tau_p^+ < 1$) deposition is effected by a combination of Brownian and eddy diffusion (regime 1), micron-sized particles ($0.1 \leq \tau_p^+ < 10$) deposit as a consequence of turbulent dispersion and growing particle inertia (regime 2), and the deposi-

tion of larger particles ($\tau_p^+ > 10$) is mainly influenced by particle inertia (regime 3) (Guha, 2008).

Most of the early numerical modelling of particle deposition in a boundary layer flow adopted the Eulerian-Lagrangian framework using either commercial computational fluid dynamic (CFD) approaches, or alternative methods, to predict the flow field. The non-CFD methods involved the development of synthetic flow and turbulence fields (Fan and Ahmadi, 1995; Kallio and Reeks, 1989; Matida et al, 2000; Swales and Reeks, 1994), whilst the commercial CFD approaches adopted a Reynolds-averaged Navier-Stokes (RANS) approach with various turbulence models (Abuzeid et al, 1991; Sun et al, 2011). Various particle dispersion models, such as the eddy interaction model, the continuous random walk model, as well as Langevin equation and random Fourier series approaches have been employed. These methods are readily used due to their low computational cost and ease of application, although they tend to over-predict by several orders of magnitude the particle deposition rate when considered against the benchmark data of (Liu and Agarwal, 1974) in regimes 1 and 2, that is for very small particles and for high Reynolds number flows. The task for researchers using a RANS modelling framework remains how to improve on the ad-hoc dispersion models available in commercial CFD codes to give results in better agreement with LES and DNS predictions.

It has been shown that accurate prediction of the flow and turbulence field in the core and in the boundary layer region is required to accurately predict the deposition rate of small particles, especially in the regimes 1 and 2 (Tian and Ahmadi, 2007). The fluid's bulk motion and turbulent diffusion are usually strong enough to rapidly transport particles from the core region to the turbulent boundary layer. Turbulent coherent structures (ejection and sweep events) within the turbulent boundary layer control particle deposition on the surface (Njobuenwu and Fairweather, 2014c). The shear lift force also has a significant effect on the deposition and

concentration of large particles close to the walls in regime 3 (Sun et al, 2011). Higher levels of accuracy when predicting particle deposition are expected when the flow field is obtained from direct numerical simulation (DNS) (Ounis et al, 1993; Zhang and Ahmadi, 2000; Zhang et al, 2001) or large eddy simulation (LES), together with sub-grid scale (SGS) velocity fluctuation contributions (Njobuenwu and Fairweather, 2014b; Salmanzadeh et al, 2010; Uijttewaal and Oliemans, 1996; Wang and Squires, 1996). Salmanzadeh et al (2010) and Njobuenwu and Fairweather (2014b) observed that the inclusion of the SGS turbulence fluctuations improves the model predictions for particle deposition rate, especially for small particles. In (Njobuenwu and Fairweather, 2014b), the shear lift force was applied for spherical particles, whilst profile lift due to particle orientation was accounted for when considering non-spherical particles. The authors obtained good agreement in regime 3 for spherical particles against the benchmark experimental data, but reported an under-prediction of the experimental deposition rate for non-spherical particles in the same regime. The non-inclusion of the shear lift force whose magnitude is of the order of the square of the particle diameter for disk and needle-like particles, and whose magnitude is higher than the drag force in the sub-viscous layer, as will be shown later in the force balance analysis, was responsible for the under-prediction.

With the recent development of a generalised shear lift force model applicable to arbitrary particle shapes in arbitrary shear flows (Ravnik et al, 2013), we improve on the deposition rate of needle and disk-like particles in regime 3 by modifying the shear lift force of (Ravnik et al, 2013). We present the effects of particle inertia and shape, and a Lagrangian force balance, on the deposition rate of non-interacting, non-spherical particles in a turbulent channel flow with a specified fluid inertia. For the flows of interest, i.e. the transport of CRUD in nuclear reactors, the flow is highly turbulent and the rotational dynamics, alignment trends and deposition of anisotropic particles (needles, platelets, near-spheres) in a turbulent boundary layer become of considerable interest. In such flows, we simulate corrosive oxides as non-spherical particles and the nuclear reactor fuel pin simplistically as the walls of a channel flow. Fluid inertia is characterised by the shear Reynolds number based on the fluid shear velocity, u_τ , and the channel half-height. The particle inertia is characterised by the particle relaxation time, τ^* .

2 Numerical methods

The particles are modelled as ellipsoids of revolution with the equation:

$$\left(\frac{x'}{a}\right)^2 + \left(\frac{y'}{b}\right)^2 + \left(\frac{z'}{c}\right)^2 = 1 \quad (1)$$

The particle shape is characterised by the aspect ratio, λ , adopting a unique type of particle anisotropy as $\lambda = c/a = c/b$, where a , b and c are the lengths of the particle semi-major axes, with c representing the principal axis. In this study, we shall analyse the deposition dynamics of ellipsoidal particles including disks ($\lambda < 1$), spheres ($\lambda = 1$), and needles or fibres ($\lambda > 1$).

To simulate non-spherical particle transport, orientation and deposition, an Eulerian-Lagrangian-Eulerian fluid-particle modelling approach has been developed (Njobuenwu and Fairweather, 2014a) and employed. The flow field is obtained using large eddy simulation of the large scale energy-containing motions with dynamic modelling of the sub-grid scale motion, in an Eulerian framework. The resulting LES transport equations were solved with the computer program BOFFIN (further details of which are given in (Njobuenwu and Fairweather, 2014a)). The channel flow, with shear a Reynolds number $Re_\tau = hu_\tau / \nu = 300$ and bulk Reynolds number $Re_b = hu_b / \nu \approx 5,000$ has inertial coordinates $\mathbf{x} = [x, y, z]$, a computational domain size $(2h \times 2h\pi \times 4h\pi)$ and grid nodes $(129 \times 128 \times 128)$ in the wall-normal, spanwise and streamwise directions, respectively.

Particle transport was treated in a Lagrangian framework and the Lagrangian force balance considered included drag, shear lift, gravity, and Brownian motion forces. We adopt a stochastic Markov model (Bini and Jones, 2008) to represent the influence of the SGS fluid velocity fluctuations experienced by a stochastic particle.

$$d\mathbf{u}_p = (\mathbf{F}_D + \mathbf{F}_{BG} + \mathbf{F}_{SL} + \mathbf{F}_{BM} + \mathbf{F}_{PL})dt + \mathbf{B} \cdot d\mathbf{W} \quad (2)$$

$$d\mathbf{x}_p = \mathbf{u}_p dt \quad (3)$$

The terms on the right hand side of Eq. (2) represent the drag (Njobuenwu and Fairweather, 2014a), buoyancy-gravity, shear lift, Brownian motion, and profile-lift forces, while the last term, representing the acceleration of the p^{th} stochastic particle by the diffusion process, is taken to be isotropic, and is given in simplified form (Bini and Jones, 2008) as $\mathbf{B} = \beta \delta_{ij}$. Here, the diffusion coefficient, β , may be expected

to depend on the time and length scales of the SGS velocity fluctuations of the continuous phase and the particle properties. Using the SGS turbulence kinetic energy, k_{sgs} , to characterise the velocity fluctuations, we may write:

$$\beta = \sqrt{C_0 k_{sgs} / \tau_t} \quad (4)$$

Here, C_0 is a model constant taken as unity (Bini and Jones, 2008), and $d\mathbf{W}$ in Eq. (2) represents the increment of the Wiener process. During the simulation, the increment of the Wiener process, $\Delta\mathbf{W}$, is represented by $\xi_i \times \sqrt{\Delta t}$, where ξ_i is a random vector sampled from a standardised Gaussian distribution, independently for each time step, Δt , and for each velocity component. τ_t in Eq. (4) is a time scale which affects the rate of interaction between the particle and the carrier phase turbulence:

$$\tau_t = \frac{\tau_p^{1.6}}{\left(\Delta / \sqrt{k_{sgs}}\right)^{0.6}} \quad (5)$$

The model has been shown to be capable of representing accurately particle dispersion in a droplet-laden turbulent mixing layer (Bini and Jones, 2008). In Eq. (5), Δ is the filter width which is given by $\Delta = (\Delta_x \Delta_y \Delta_z)^{1/3}$. The SGS turbulence kinetic energy is obtained using equilibrium arguments from:

$$k_{sgs} = (2\Delta \nu_{sgs} S_{ij} S_{ij})^{\frac{2}{3}} \quad (6)$$

The particle shape and orientation are accounted for by solving Euler's equation of rotational motion with Euler quaternions representing the particle orientation (Njobuenwu and Fairweather, 2014a):

$$\frac{d\omega_{x'}}{dt} = \frac{T_{x'}}{I_{x'x'}} + \left(\frac{I_{y'y'} - I_{z'z'}}{I_{x'x'}} \right) \omega_{y'} \omega_{z'} \quad (7)$$

$$\frac{d\mathbf{q}}{dt} = \begin{pmatrix} \dot{q}_0 \\ \dot{q}_1 \\ \dot{q}_2 \\ \dot{q}_3 \end{pmatrix} = \frac{1}{2} \begin{bmatrix} q_0 & -q_1 & -q_2 & -q_3 \\ q_1 & q_0 & -q_3 & q_2 \\ q_2 & q_3 & q_0 & -q_1 \\ q_3 & -q_2 & q_1 & q_0 \end{bmatrix} \begin{bmatrix} 0 \\ \omega_{x'} \\ \omega_{y'} \\ \omega_{z'} \end{bmatrix} \quad (8)$$

Note that the equations for translational motion are expressed in the inertial frame $\mathbf{x} = [x, y, z]$, while rotational motions are written in the particle frame $\mathbf{x}' = [x', y', z']$. The transformation between these frames of reference is given by $\mathbf{X}' = \mathbf{A}\mathbf{X}$, where $\mathbf{A} = [a_{ij}]$ is the transformation matrix, whose elements represent the four Euler quaternions, $\mathbf{q} = [q_0, q_1, q_2, q_3]$:

$$\mathbf{A} = \begin{bmatrix} 1 - 2(q_2^2 + q_3^2) & 2(q_1 q_2 + q_3 q_0) & 2(q_1 q_3 - q_2 q_0) \\ 2(q_2 q_1 - q_3 q_0) & 1 - 2(q_3^2 + q_1^2) & 2(q_2 q_3 + q_1 q_0) \\ 2(q_3 q_1 + q_2 q_0) & 2(q_3 q_2 - q_1 q_0) & 1 - 2(q_1^2 + q_2^2) \end{bmatrix} \quad (9)$$

A fourth order Runge-Kutta scheme is applied to solve the Newton equation of motion to give the particle position and velocity, and the Euler equation of rotation to yield the particle orientation and rotation.

Particle deposition is defined here as the process of attaching suspended particles from a fluid in motion to the surface of the wall. For deposition to occur, the particle is assumed to have contact with the wall surface and to adhere to the wall at the point of contact. The particle wall boundary condition is straightforward for spherical particles, and complex for non-spherical particles. Spherical particles are assumed to have contacted the wall when the distance from their centre of mass to the wall is less than the particle radius. However, for anisotropic particles, three deposition scenarios can occur (Fan and Ahmadi, 1995). First, if the distance of the particle centroid from the boundary surface is less than the semi-minor axis, a , it will be deposited. Second, if this relative position is greater than the semi-major axis, c , the ellipsoid is in suspension. Third, when the distance between the particle centroid and the wall is within the range of the a and c axes, whether the ellipsoid is deposited or not depends on its orientation relative to the wall.

The particle to fluid density ratio was set to $S = \rho_p / \rho = 770$ which represents the density ratio used in the olive oil in air experiments of Liu and Agarwal (1974). Several thousand particles $O(10^5)$ with a diameter range 0.1 – 300 μm were uniformly distributed at the inlet of the channel, with their initial linear and rotational velocity equal to those of the fluid at the particle position. The particle initial orientation was specified randomly by Euler angles. The number of particles used was found to be sufficiently large to provide stationary statistics. Of particular interest is the number of particles deposited, and the particle deposition rate was monitored as a fractional penetration, as reported by Liu and Agarwal (1974). Using these data, the deposition rate was calculated for each particle size and shape using (Gao and He, 2012):

$$u_d = \ln\left(\frac{N_0}{N_{out}}\right) \frac{U_b L_x}{L_z} = \ln\left(\frac{N_0}{N_0 - N_d}\right) \frac{U_b L_x}{L_z} \quad (10)$$

where N_d is the number of particles deposited onto the walls, U_b is the bulk air velocity, L_z is the length of the channel section where deposi-

tion is studied, and L_x is the height of the channel. Therefore, the time required to flush particles through the channel should be L_z/U_b , and not the maximum computing time as used by other authors. At the inlet, $N = N_0$, whilst at the outlet, $N = N_{out}$, with $N_{out} = N_0 - N_d$. The non-dimensional deposition velocity, $u_d^+ = u_d/u_\tau$, is usually reported in terms of the non-dimensional response time, defined for spherical particles as:

$$\tau_d^+ = \frac{2Sa^{+2}}{9}, \quad a^+ = \frac{au_\tau}{\nu} \quad (11)$$

where a is the semi-minor axis and represents the radius of a spherical particle. Eq. (11) requires modification for non-spherical particles and, although several modifications are available, we adopt that based on the equivalent volume of sphere diameter, $d_{eq} = 2a\lambda^{1/3}$, giving the corresponding particle response time as:

$$\tau_{eq}^+ = \tau_d^+ \lambda^{2/3} \quad (12)$$

3 Results and discussion

The LES of turbulent channel flow and Lagrangian particle tracking of non-spherical inertial particles has been shown previously (Njobuenwu and Fairweather, 2013a) to be in good agreement with DNS-based results. Prediction of particle deposition with varying particle aspect ratio, for a disk ($\lambda = 0.1$), sphere ($\lambda = 1$) and needle-like ($\lambda = 3, 10, 30$ and 50) particles, is reported below.

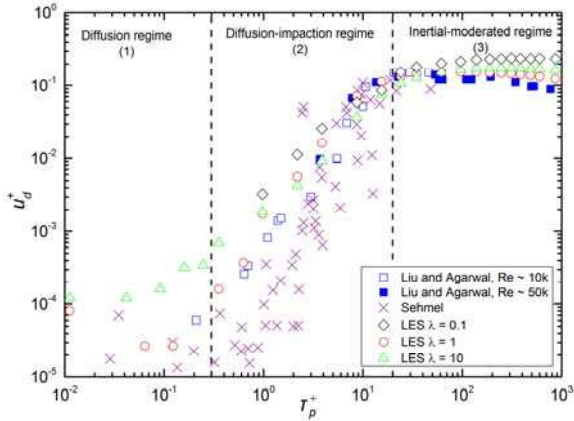


Figure 1: Comparison of predicted deposition velocity with available data for spherical ($\lambda=1.0$), disk ($\lambda = 0.1$) and needle-like ($\lambda = 10$) particles.

Figure 1 shows the non-dimensional deposition velocity, u_d^+ , against the non-dimensional equivalent particle relaxation time, τ_{eq}^+ . The LES and the Lagrangian force balance adopted predict the classic “S-shaped” curve with good

agreement with the Liu and Agarwal (1974) data, and with reasonable qualitative agreement with the Sehmel (1968) data, for spheres. This agreement is acceptable since Guha (2008) has reported a wide scatter in the deposition rate data, as can be seen by comparing the Liu and Agarwal (1974) and Sehmel (1968) data. The disk and needle-like particles generally exhibit a higher deposition rate than spherical particles of equal equivalent volume sphere relaxation time, while the disk particles have in turn an increased deposition rate relative to the needle-like particles. The ellipsoidal particles have been reported to have a higher dispersion than for spheres (Njobuenwu and Fairweather, 2014a), and are expected to have a higher probability of contacting with the wall surface than their spherical counterparts because of their rotational dynamics (Njobuenwu and Fairweather, 2013b).

In Figure 2 the probability density function (PDF) of selected translational properties is shown for anisotropic particles with aspect ratios $\lambda > 1$. In order to reduce scatter in the results, the number of particles examined was increased from 100k to 500k, and the use of 500k particles applies to the rest of the results shown below, unless otherwise stated. In Figure 2 it is clear that particle shape influences the position of the particle centroid in the wall-normal direction when deposition occurs. For a $Re_\tau = 300$ flow, a prolate particle with aspect ratio $\lambda < 10$ deposits on the wall when its centroid is within the viscous sub-layer, while for more elongated particles, the position of the centre of mass falls within the viscous sub-layer and buffer layers ($x^+ < 30$). The horizontal axis of Figure 2 showing wall-normal position indicates that the distance of the particle centroid from the surface is less than both the semi-minor axis, a , and the semi-major axis, c . Particles are more likely to deposit on the wall when they are in the near-wall region and when they align with the wall-normal axis, i.e. when the angle between the particle principal axis and the x -axis is 0 or π . This tendency increases with particle elongation.

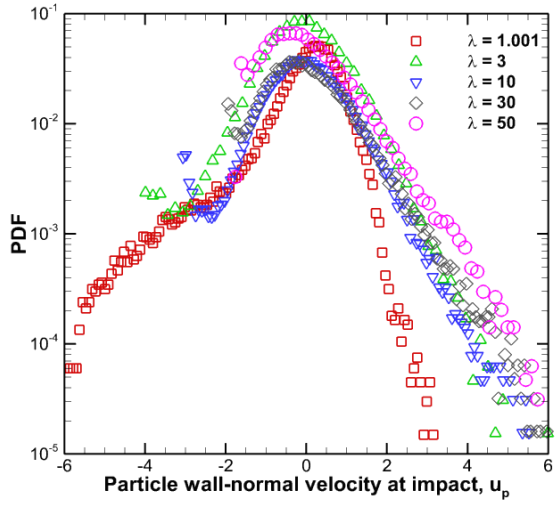
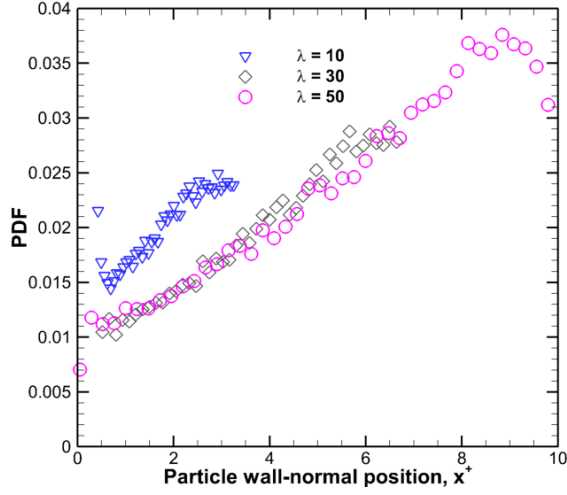


Figure 2: PDF of particle wall-normal translational properties at impact with the wall: position, x^+ (top) and velocity (bottom).

Also in Figure 2, the PDF of the magnitude of the particle wall-normal velocity component u_p at deposition is normalised as $Z = (u_p - \langle u_p \rangle) / u'_{p,rms}$ (where $\langle u_p \rangle$ and $u'_{p,rms}$ are the mean velocity and root-mean-square of the velocity fluctuations) to visualise the PDF tail. The results clearly show a trend in terms of the tail of the PDF. As expected, the spread of the tail increases for prolate spheroids with an increasingly elongated shape since the position of the centroid spans the viscous sub-layer and buffer layer. The peak of the PDF of the velocity occurs at a similar value for particles with aspect ratios $\lambda = 3, 10$ and 30 , although this peak shifts slightly to the right for prolate spheroids with small aspect ratio, i.e. close to spherical ($\lambda = 1.001$), and to the left for very elongated ($\lambda = 50$) particles.

The distribution of particle direction cosines, $\cos\theta_x$, $\cos\theta_y$ and $\cos\theta_z$, at the point of particle

deposition on the surface is shown in Figure 3 to illustrate the influence of aspect ratio on such deposition (for $\lambda > 1$ particles). Note that the spheroid major axis, z' , is perpendicular to the x, y and z axes when $\cos\theta_x = 0$, $\cos\theta_y = 0$ and $\cos\theta_z = 0$, and parallel to the same axes when $|\cos\theta_x| = 1$, $|\cos\theta_y| = 1$ and $|\cos\theta_z| = 1$. As expected, for the particle with an aspect ratio close to spherical, there is no preferential orientation at or even before deposition, hence, it exhibits the same value of the PDF for all orientations with respect to the three axes. For aspect ratios ranging from 3 to 50, the PDF exhibits increasing values at $|\cos\theta_x| \sim 1$, and decreasing values at $\cos\theta_x = 0$, with increases in aspect ratio (top). However, the $\lambda = 3$ particle shows the largest PDF, and this may be a critical aspect ratio for such observations. In the centre panel, apart from particles with $\lambda = 1.001$, the principal z' axis is more normal to the vorticity (y) axis, with a reduced tendency to align with that axis. The particle with $\lambda = 3$ also shows the highest values at $\cos\theta_x = 0$. In the lower panel of Figure 3, only the particle with aspect ratio $\lambda = 3$ shows a strong alignment with the direction of the flow (z -axis) at the time of deposition, hence its PDF is highest at $|\cos\theta_x| \sim 1$. The highest position of its centroid at the point of deposition falls in the viscous sub-layer, which is below the region where velocity streaks are observed. The other particles show no preferential alignment with respect to the flow direction at the point of deposition.

The position and orientation (for non-spherical cases) of particles on the lower and upper wall surfaces is shown in Figure 4 for various shapes of particles, with both sets of non-spherical results having an equal equivalent sphere diameter, $d_{eq} = 100 \mu\text{m}$, and a dimensionless particle relaxation time $\tau_p^+ = 96$. These results clearly illustrate the importance of shape to how particles deposit on a surface and, ultimately, how they form particle beds that may block a flow or affect heat transfer rates. The deposition pattern indicates the contact mode for the different shapes. The number of particles deposited is highest at the inlet of the channel, and the particles form streaks, with dense and sparse regions occurring for all three aspect ratios.

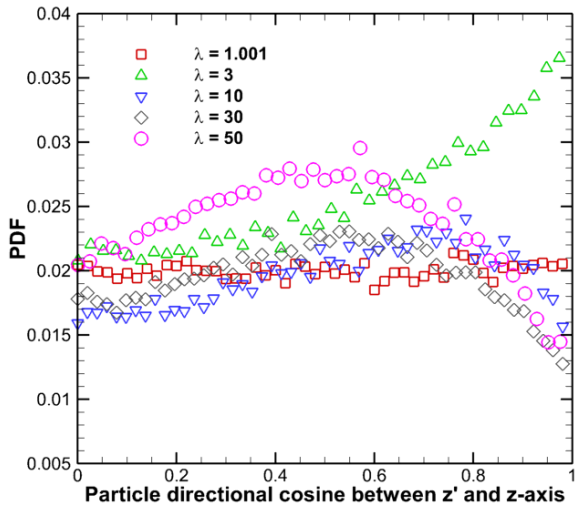
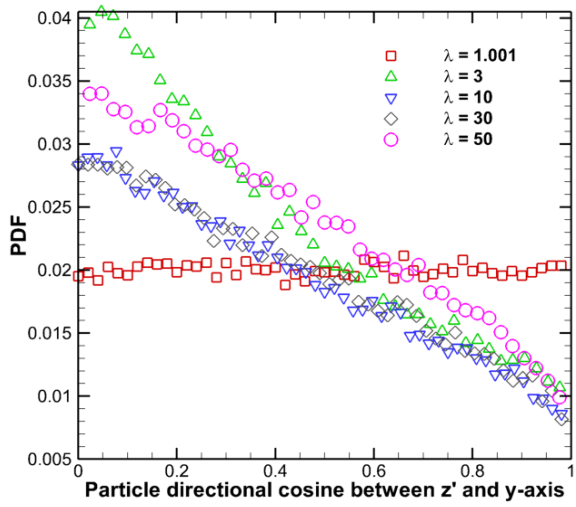
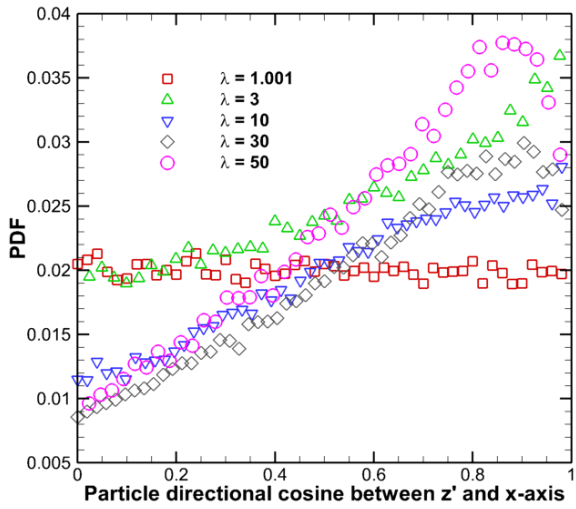


Figure 3: Particle directional cosines between principal z' axis and fixed (inertial) frame at the point of wall deposition.

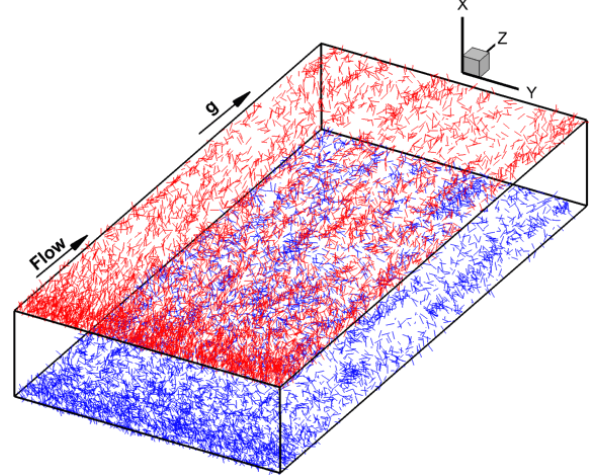
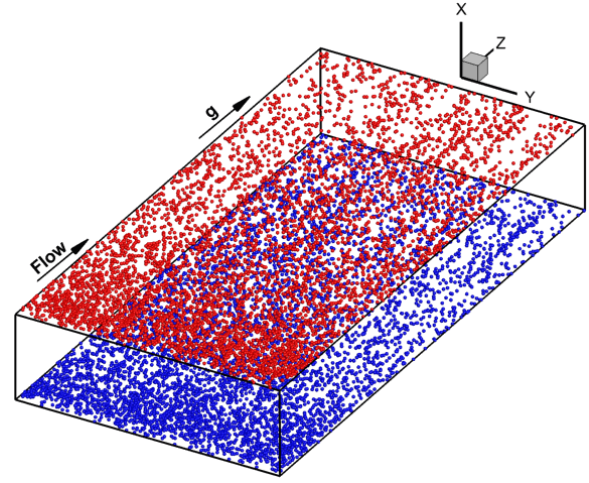
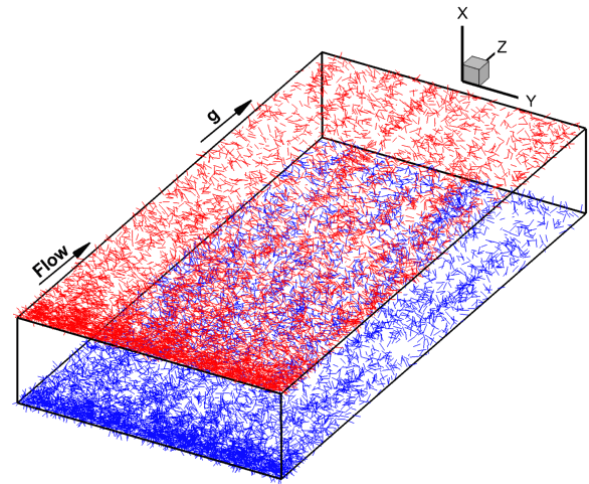


Figure 4: Deposition pattern of disk (top), spherical (middle) and needle-like (bottom) particles on wall (note in top, line represents disk diameter).

Lastly, Table 1 shows the relative magnitude of each of the shear lift force, the profile lift force (for non-spherical particles) and the stochastic (Brownian motion) force term with respect to the deterministic drag force in three representative boundary layer regions in the channel, i.e. the viscous sub-layer, the buffer region and the inertial region. Only the wall-normal component of these forces is considered,

hence, the buoyancy-gravity force is not included since it acts along the streamwise direction. The integral drag force, F_D , the lift (shear, F_{SL} , and profile, F_{PL}) forces, and the Brownian motion force, F_{BM} , in each boundary layer region were calculated by summing the absolute values of the respective force components in the wall-normal direction for all particles in that region.

There are clear trends in the results of Table 1, where the shear lift force is larger than the drag force for all particle shapes with equivalent sphere diameter $d_{eq} = 100 \mu\text{m}$ in the viscous sub-layer region. As expected, the Brownian force is smaller than the drag force for such micro-sized particles, although it is expected to be the dominant force for smaller-sized particles of $d_{eq} \leq 1 \mu\text{m}$. However, the effect of F_{BM} is seen to decrease as the particle aspect ratio increases over the entire boundary layer region. This indicates that deposition due to Brownian diffusion for micro-sized prolate particles also reduces as the particle aspect ratio is increased. The profile lift is non-existent for the spherical particle, but its effect is decreased with increases in aspect ratio for the prolate particle, except for the particle with aspect ratio $\lambda = 3$ which has the largest profile lift force of any particle over the entire boundary layer region.

4 Conclusions

The deposition of disk-shaped, spherical and needle-like particles in a vertical channel was investigated using large eddy simulation and a Lagrangian particle tracking scheme coupled to the Euler rotation equation. A force balance comprising the deterministic and stochastic force terms acting on a particle, and which caters for the wide range of particle sizes studied, was employed. The overall approach was found to be able to reliably predict the classic "S-shaped" curve which describes the variation of particle deposition velocity with equivalent particle relaxation time established through experiment for spherical particles. The work reported also demonstrates that different particle shapes have different deposition patterns, and the inclusion of particle orientation effects ensures that these patterns are captured.

Acknowledgements

The authors wish to thank the Engineering and Physical Sciences Research Council for their financial support of the work reported in this paper under EPSRC Grant EP/I003010/1, "Computational Modelling for Advanced Nuclear Power Plants".

References

- Abuzeid, S., Busnaina, A.A., Ahmadi, G. (1991), Wall deposition of aerosol particles in a turbulent channel flow. *J. Aerosol Sci.*, Vol. 22, pp. 43-62.
- Bini, M., Jones, W.P. (2008), Large-eddy simulation of particle-laden turbulent flows. *J. Fluid Mech.*, Vol. 614, pp. 207-252.
- Fan, F.-G., Ahmadi, G. (1995), A sublayer model for wall deposition of ellipsoidal particles in turbulent streams. *J. Aerosol Sci.*, Vol. 26, pp. 813-840.
- Gao, N., He, Q. (2012), Calculation of particle deposition velocity in the Lagrangian frame. *Indoor Built Environ.*, Vol. 21, pp. 348-350.
- Guha, A. (2008), Transport and deposition of particles in turbulent and laminar flow. *Annu. Rev. Fluid Mech.*, Vol. 40, pp. 311-341.
- Hazleton, R.F. (1987) Characteristics of fuel crud and its impact on storage, handling, and shipment of spent fuel: Pacific Northwest Lab PNL-6273, DE88 000914.
- Kallio, G.A., Reeks, M.W. (1989), A numerical simulation of particle deposition in turbulent boundary layers. *Int. J. Multiphas. Flow*, Vol. 15, pp. 433-446.
- Liu, B.Y.H., Agarwal, J.K. (1974), Experimental observation of aerosol deposition in turbulent flow. *J. Aerosol Sci.*, Vol. 5, pp. 145-155.
- Matida, E.A., Nishino, K., Torii, K. (2000), Statistical simulation of particle deposition on the wall from turbulent dispersed pipe flow. *Int. J. Heat Fluid Flow*, Vol. 21, pp. 389-402.
- Njobuenwu, D.O., Fairweather, M. (2012), Modelling of pipe bend erosion by dilute particle suspensions. *Comput. Chem. Eng.*, Vol. 42, pp. 235-247.
- Njobuenwu, D.O., Fairweather, M. (2013a), Inertial particle behaviour in turbulent fluid flow. In: Andrzej, K., Ilkka, T., Eds., *Comp. Aided Chem. Eng.* 32: Elsevier, pp 253-258.
- Njobuenwu, D.O., Fairweather, M. (2013b), Non-spherical particle translation and orientation in wall-bounded turbulence, In: Simos, T., Psihoyios, G., Tsitouras, C., Eds., *11th Int. Conf. Numerical Analysis and Applied Mathematics*. Rhodes, Greece: AIP Conf. Proc., Vol. 1558, pp 132-135.
- Njobuenwu, D.O., Fairweather, M. (2014a), Effect of shape on inertial particle dynamics in a channel flow. *Flow Turbulence Combust.*, Vol. 92, pp. 83-101.
- Njobuenwu, D.O., Fairweather, M. (2014b), Large eddy simulation of non-spherical particle

deposition in a vertical turbulent channel flow. In: Klemeš, J.J., Varbanoc, P.S., Liew, P.Y., Eds., *Comput. Aided Chem. Eng.* 33: Elsevier, pp 907-912.

Njobuenwu, D.O., Fairweather, M. (2014c), Quadrant and conditional analyses of non-spherical particle segregation in a turbulent channel flow, *7th World Congress on Particle Technology (WCPT7)*. Beijing, China, 19th-22nd May 2014.

Ounis, H., Ahmadi, G., McLaughlin, J.B. (1993), Brownian particle deposition in a directly simulated turbulent channel flow. *Phys. Fluids*, Vol. 5, pp. 1427-1432.

Ravnik, J., Marchioli, C., Hribersek, M., Soldati, A. (2013), On shear lift force modelling for non-spherical particles in turbulent flows, *11th Int. Conf. Numerical Analysis and Applied Mathematics*. Rhodos, Greece: AIP Conf. Proc., Vol. 1558, pp 1107-1110.

Salmanzadeh, M., Rahnama, M., Ahmadi, G. (2010), Effect of sub-grid scales on large eddy simulation of particle deposition in a turbulent channel flow. *Aerosol Sci. Technol.*, Vol. 44, pp. 796-806.

Sehmel, G.A. (1968), Aerosol deposition from turbulent airstreams in vertical conduits: Pacific Northwest Lab., Battelle-Northwest, BNWL-578.

Sun, K., Lu, L., Jiang, H. (2011), Modelling of particle deposition and rebound behaviour on

ventilation ducting wall using an improved wall model. *Indoor Built Environ.*, Vol. 20, pp. 300-312.

Swailles, D.C., Reeks, M.W. (1994), Particle deposition from a turbulent flow. I. A steady-state model for high inertia particles. *Phys. Fluids*, Vol. 6, pp. 3392-3403.

Tian, L., Ahmadi, G. (2007), Particle deposition in turbulent duct flows-comparisons of different model predictions. *J. Aerosol Sci.*, Vol. 38, pp. 377-397.

Uijttewaal, W.S.J., Oliemans, R.V.A. (1996), Particle dispersion and deposition in direct numerical and large eddy simulations of vertical pipe flows. *Phys. Fluids*, Vol. 8, pp. 2590-2604.

Wang, Q., Squires, K.D. (1996), Large eddy simulation of particle deposition in a vertical turbulent channel flow. *Int. J. Multiphas. Flow*, Vol. 22, pp. 667-683.

Zhang, H., Ahmadi, G. (2000), Aerosol particle transport and deposition in vertical and horizontal turbulent duct flows. *J. Fluid Mech.*, Vol. 406, pp. 55-80.

Zhang, H., Ahmadi, G., Fan, F.-G., McLaughlin, J.B. (2001), Ellipsoidal particles transport and deposition in turbulent channel flows. *Int. J. Multiphas. Flow*, Vol. 27, pp. 971-1009.

Table 1: Magnitude of the shear lift, Brownian motion and profile lift forces for particles ($\tau_p^+ = 96.44$) with aspect ratios $\lambda \geq 1$ at three different boundary layer locations.

λ	Viscous sub-layer ($x^+ < 5$)			Buffer region ($5 \leq x^+ < 30$)			Inertial region ($x > 0.2h$)		
	F_{SL}/F_D	F_{BM}/F_D	F_{PL}/F_D	F_{SL}/F_D	F_{BM}/F_D	F_{PL}/F_D	F_{SL}/F_D	F_{BM}/F_D	F_{PL}/F_D
1	3.27	1.49×10^{-3}	0.00	9.79×10^{-1}	1.92×10^{-3}	0.00	6.23×10^{-2}	1.56×10^{-3}	0.00
1.001	3.56	9.00×10^{-4}	9.71×10^{-3}	1.30	1.46×10^{-3}	9.53×10^{-3}	9.68×10^{-2}	1.29×10^{-3}	4.95×10^{-3}
3	2.53	6.70×10^{-4}	1.15×10^{-2}	9.14×10^{-1}	1.04×10^{-3}	1.04×10^{-2}	7.97×10^{-2}	9.13×10^{-4}	5.00×10^{-3}
10	1.80	4.29×10^{-4}	9.22×10^{-3}	7.09×10^{-1}	6.48×10^{-4}	9.79×10^{-3}	8.04×10^{-2}	5.71×10^{-4}	5.07×10^{-3}
30	1.59	2.65×10^{-4}	3.65×10^{-3}	7.02×10^{-1}	4.54×10^{-4}	9.56×10^{-3}	1.09×10^{-1}	4.03×10^{-4}	5.31×10^{-3}
50	1.57	1.55×10^{-4}	2.38×10^{-3}	7.40×10^{-1}	3.22×10^{-4}	8.31×10^{-3}	1.31×10^{-1}	2.87×10^{-4}	5.66×10^{-3}